HHS Public Access

Author manuscript

Curr Biol. Author manuscript; available in PMC 2023 July 25.

Published in final edited form as:

Curr Biol. 2022 July 25; 32(14): 3110–3120.e6. doi:10.1016/j.cub.2022.06.023.

Functional convergence of on-off direction selective ganglion cells in the visual thalamus

Qiufen Jiang[1,*], **Elizabeth Y. Litvina**[1,2,*], **Héctor Acarón Ledesma**[1], **Guanhua Shu**[1], **Takuma Sonoda**[1], **Wei Wei**[3], **Chinfei Chen**[1,4,#]

[1]F.M. Kirby Neurobiology Center, Boston Children's Hospital, Harvard Medical School, 3 Blackfan Circle, Boston, MA 02115, USA

[2]National Institute of Neurological Disorders and Stroke, 6001 Executive Boulevard Suite 3309 Bethesda, MD 20824, USA

[3]Department of Neurobiology, The University of Chicago, 947 East 58th Street, Chicago, Illinois 60637, USA

[4]Lead contact

Summary

In the mouse visual system, multiple types of retinal ganglion cells (RGCs) each encode distinct features of the visual space. A clear understanding of how this information is parsed in their downstream target, the dorsolateral geniculate nucleus (dLGN), remains elusive. Here, we characterized retinogeniculate connectivity in *Cart-IRES2-Cre-D* and *BD-CreER2* mice, which label subsets of on-off Direction Selective Ganglion Cells (ooDSGCs) tuned to the vertical directions and to only ventral motion, respectively. Our immunohistochemical, electrophysiological, and optogenetic experiments reveal that only a small fraction (< 15%) of thalamocortical (TC) neurons in the dLGN receive primary retinal drive from these subtypes of ooDSGCs. The majority of the functionally identifiable ooDSGC inputs in the dLGN are weak and converge together with inputs from other RGC types. Yet our modeling indicates that this mixing is not random: BD-CreER^{+} ooDSGC inputs converge less frequently with ooDSGCs tuned to the opposite direction than with non-CART-Cre^{+} RGC types. Taken together, these

[#]Correspondence: Chinfei.Chen@childrens.harvard.edu, Contact Information: Chinfei Chen, Department of Neurology, F.M. Kirby Neurobiology Center, Children's Hospital Boston, 3 Blackfan Circle, Center for Life Sciences, CLS12250, Boston, MA 02115.

[*]Equal first authors

Author contributions

Q.J., E.Y.L., and C.C. designed the experiments and wrote the paper. W.W. and H.A. designed the retinal imaging experiments and summarized the description and results of these experiments in the manuscript. H.A. conducted calcium imaging experiments for the retinas of *Cart;GCaMP6f* mice. G.S. performed the immunostaining of mouse retinas and dLGN slices. Q.J. and E.L. conducted the whole-cell patch recordings from dLGN neurons. T.S. did the enucleation surgeries and collected the samples. This work was conducted while E.Y.L. was employed at Children's Hospital Boston. E.Y.L. edited parts of the manuscript while employed by NINDS. The opinions expressed in this article are the author's own and do not reflect the view of the National Institutes of Health, the Department of Health and Human Services, or the United States government.

Declaration of interests

The authors declare no competing interests.

results indicate that convergence of distinct information lines in dLGN follow specific rules of organization.

eTOC Blurb

Jiang, Litvina *et al.* explore the rules of convergence among inputs from different types or subtypes of RGCs onto thalamocortical neurons in visual thalamus. They identify a specific wiring organization for on-off direction selective retinal inputs. Their results show that distinct rules apply for RGC types vs. subtypes.

Graphical Abstract

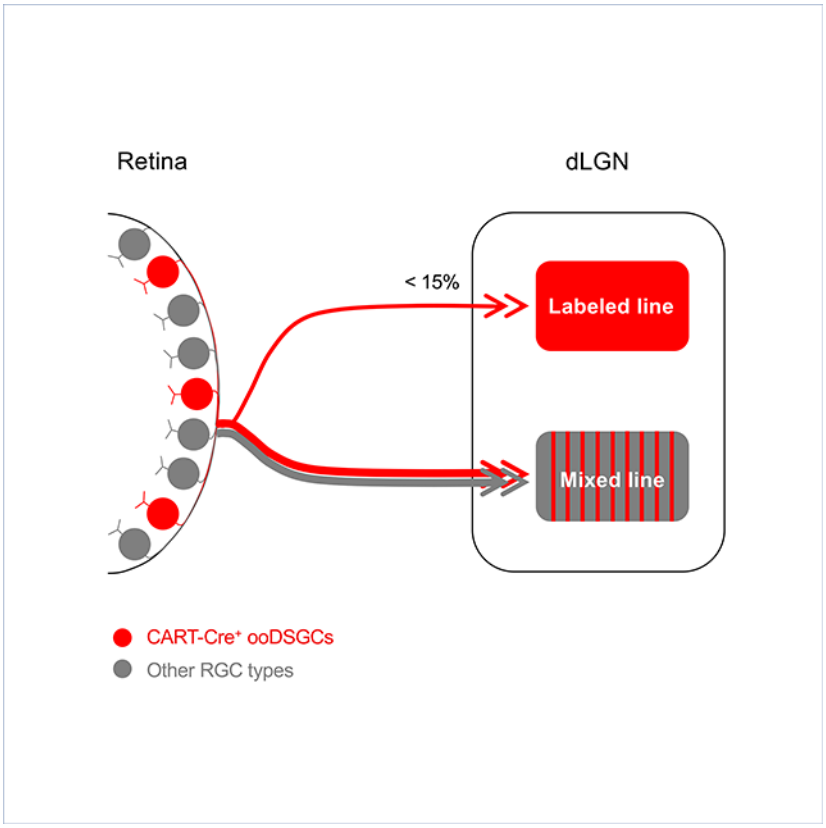

Keywords

Retinogeniculate synapse; information processing; thalamus; sensory integration; labeled lines

Introduction

Understanding the circuit mechanisms underlying the integration of information in the central nervous system has been key to progress in neuroscience. An emerging experimental model for studying this question is the mouse retinogeniculate synapse: the connection between retinal ganglion cells (RGCs) in the eye and thalamocortical (TC) relay neurons in the visual thalamus. In mouse, at least 40 distinct types of RGCs encoding different

visual features have been described based on their unique combination of morphological, genetic, and physiological properties[1–7]. One prominent feature of the mouse retina is the on-off direction-selective circuit in which the output neurons, the on- off direction-selective ganglion cells (ooDSGCs), responds to both increments and decrements of light and fires maximally to motion along one particular direction. ooDSGCs comprise about 15% of the total RGC population[8, 9] and can be classified into 4 subtypes, each tuned to one of four cardinal axes: dorsal (downward in visual field), ventral (upward), nasal (posterior), or temporal (anterior)[3, 9–12]. OoDSGCs play a fundamental role in detecting alterations in light intensity and stimulus motion that is critical for behavior[4, 13].

In mice, ooDSGCs project to the dorsal lateral geniculate nucleus (dLGN) in the image-forming pathway, raising questions of whether and how this information is parsed on its way to the cortex. The traditional view is that visual information is relayed from retina to cortex along “labeled lines”, such that the feature selectivity of a RGC type matches that of the TC neuron it innervates[14, 15]. However, recent studies have shown that RGC inputs with different features can converge onto the same TC neuron, implying a greater degree of integration in this thalamic “relay station” than previously recognized[16–19]. Little is known of how the synaptic organization of ooDSGCs in the dLGN maps onto these two opposing schema: both evidence that ooDSGC signals can occupy distinct “labeled lines” and integrate with other retinal information streams have been reported[16, 19]. However, these studies focused on presynaptic activity or rabies virus labeling, rather than directly assessing synaptic function. Here, we took advantage of available genetic tools to examine both the anatomical and functional relevance and relative prevalence of these two schema using optogenetics to identify ooDSGC inputs.

To determine whether inputs that are tuned to different directions exhibit similar synaptic properties and weights, we take advantage of two Cre-expressing transgenic mouse lines that identify different subtypes of ooDSGCs, one a subset of the other. The cocaine- and amphetamine-regulated transcript neuropeptide (CART; gene symbol *Cartpt*) is selectively expressed in three ooDSGC subtypes tuned to dorsal, ventral, or nasal motion[8, 20]. The *Cart-IRES2-Cre-D* mouse line was, therefore, used to simultaneously label multiple subtypes of ooDSGCs[12]. The *BD-CreER* mouse is a tamoxifen-dependent line that labels one subtype of this population: ooDSGCs tuned to ventral motion in the retina. In this study, we characterize and compare the anatomical and synaptic properties of these two sets of ooDSGCs in the dLGN. Axon labeling analysis and electrophysiological studies reveal that these two sets make functional connections in the same region of the dLGN. However, BD-CreER$^+$ inputs tend not to converge onto the same postsynaptic TC neurons with the other (oppositely-tuned) CART-Cre$^+$ ooDSGC inputs. Instead, CART-Cre$^+$ or BD-CreER$^+$ ooDSGC inputs preferentially converge with other RGC type inputs. Moreover, only a small fraction of TC neurons receive more than 50% of their drive from BD-CreER$^+$ or CART-Cre$^+$ inputs. Our findings suggest that there are specific rules for the convergence of information lines coding distinct aspects of the visual space.

Results

Specific expression of ChR2 in CART$^+$ RGCs

To assess the functional contributions of distinct ooDSGCs in the dLGN, we aimed to selectively label axons of RGC subsets tuned to different directions[2, 8]. Of the different available *Cart-Cre* mouse lines, we characterized *Cart-IRES2-Cre-D* ("*Cart-Cre*") by crossing the line with Cre-dependent GCaMP6f mice (*Ai95D*). Calcium responses to bars moving along eight directions were recorded from CART-Cre$^+$ RGCs expressing GCaMP6f (Figure 1A, see STAR Methods). *Cart-cre* mainly label ooDSGCs tuned to the vertical directions with 50.6 % preferring dorsal and 49.4 % preferring ventral motion (Figures 1B and S1). In contrast, BD-CreER$^+$ RGCs have been previously characterized as labeling just one CART$^+$ RGC subtype, tuned to ventral motion[8, 21]. We therefore chose these two lines for further studies.

We next assessed channelrhodopsin-2 (ChR2) expression in retinas of P30 *Cart-Cre* or *BD-CreER* mice crossed with Cre-dependent ChR2-EYFP expressing mice, *Ai32* (termed "*Cart;ChR2*" and "*BD;ChR2*" mice, respectively). Consistent with previous reports, immunostaining demonstrated labeling of assorted retinal cells, including RGCs, glial cells and putative amacrine cells in the *Cart;ChR2* retinas (Figure 1C$_1$ left)[2, 22]. As only RGCs project out of the retina to the dLGN, we focused on the specificity of the *Cart;ChR2* RGC type labeling, using RBPMS to identify RGCs. In *Cart;ChR2* mice, 91.46±2.33% of GFP$^+$ (CART-Cre$^+$) RGCs in the ganglion cell layer co-immunostained with CART (n = 4 mice), demonstrating a high degree of specificity of ChR2 labeling (Figure 1C$_2$ left). However, only ~half (53.92±1.07%) of CART-immunoreactive (CART$^+$) RGCs (RBPMS$^+$) expressed GFP (Figure 1C$_2$ right), consistent with our finding that *Cart;ChR2* labels only the subtypes of CART-expressing ooDSGCs preferring vertical motion (Figure 1B) and that dorsally and ventrally tuned ooDSGCs comprise ~50% of all CART$^+$ RGCs[12].

A similar analysis in the retina of *BD;ChR2* mice revealed a high proportion of GFP$^+$ (BD-CreER$^+$) RGCs that expressed CART (93.82±1.84%, n = 5 mice) (Figures 1D$_1$ and 1D$_2$ left), consistent BD RGCs being a subtype of CART ooDSGC. Among the CART$^+$ RGCs, 34.59±3.72% expressed GFP in the retina of *BD;ChR2* mice (Figure 1D$_2$ right). Due to lack of antibodies specific for labelling BD RGCs, we were not able to quantify the efficiency of ChR2 labelling in BD RGCs. Overall, these data demonstrated that ChR2 expression among axons leaving the retina in both mouse lines are largely restricted to ooDSGCs.

To discern labeling of retinal projections from other potential sources, we examined colocalization of ChR2-tagged GFP and VGluT2 (a presynaptic marker for RGC inputs[23]) in the dLGN. In both mouse lines, GFP$^+$ axonal boutons exhibit a high degree of overlap with VGluT2 immunostaining (Figure 1E). Furthermore, binocular enucleation completely removed ChR2 labeling from dLGN for both mouse lines (Figure 1F), indicating that retina is its sole source. Together, these data support the use of *Cart;ChR2* and *BD;ChR2* mice to selectively label, activate and compare the TC neuron response to these two sets of CART$^+$ ooDSGCs inputs.

Anatomical organization of CART-Cre$^+$ and BD-CreER$^+$ inputs in the dLGN

We next compared RGC axonal territories in the dLGN of the two mouse lines. In coronal sections of the dLGN of *Cart;ChR2* mice, GFP$^+$ RGC axons could be observed to terminate densely in the dorsal aspect bordering the ventricle and extend deeper into the nucleus when moving along anterior-posterior axis (Figure 2A left). The axonal labeling of GFP$^+$ RGCs from *BD;ChR2* mice overlapped largely with the territory of CART-Cre$^+$ terminals with the exception of the most dorsal edge of the dLGN (Figure 2A right). To compare the spatial distribution of terminal endings between CART-Cre$^+$ and BD-CreER$^+$ axons, we collapsed the two-dimensional dLGN area into a one-dimensional line plot by summing the signals of maximal intensity projections along the lateral-to-medial axis of the coronal slice (Figure S2B top, see STAR Methods). The line plots confirmed the overlap of spatial territory between CART-Cre$^+$ and BD-CreER$^+$ inputs in a deeper area of dLGN, as expected given that BD-CreER$^+$ RGCs comprise a subset of CART-Cre$^+$ ooDSGCs (Figure S2B bottom). Taken together, when compared with the distribution of axonal terminals in *Cart;ChR2* mice, BD-CreER$^+$ inputs were sparser and concentrated in a subregion of the occupied territory.

Functional organization of CART-Cre$^+$ and BD-CreER$^+$ inputs in dLGN

Our (Figure 2) and published[2, 8, 24–27] data indicate that both CART and BD RGCs preferentially project to dLGN “shell” region. Since retinal inputs synapse on the proximal dendrites of TC neurons[17, 28–33], the anatomical distribution of RGC axons in dLGN should map well with the distribution of functional inputs onto TC neurons. Thus we examined the functional connectivity of CART-Cre$^+$ and BD-CreER$^+$ ooDSGCs in their overlapping territory in the dLGN. To assess the strength and spatial distribution of retinogeniculate drive from CART-Cre$^+$ and BD-CreER$^+$ RGCs, we used an established parasagittal slice preparation of the dLGN (see STAR Methods), optimized for physiology because it preserves the retinal axon arbors[34–36]. We first compared the expression of ChR2 from this parasagittal view and found that BD-CreER$^+$ terminals overlap with a subset of CART-Cre$^+$ terminals in the ventral-posterior territory (Figures 2B and S2C, see STAR Methods).

Then we performed whole-cell patch clamp recordings of randomly sampled TC neurons from the ventral-posterior area (Figure 2B lateral and middle sections). We recorded maximal excitatory post-synaptic currents, optically evoked using full-field blue light illumination (oEPSCs) (Figure 3A), and by adding bicuculline ($GABA_AR$ antagonist), CGP55845 ($GABA_BR$ antagonist), DPCPX (antagonist of A1 adenosine receptors) and LY341495 (antagonist of presynaptic group II mGluRs) in the bath solution (see STAR Methods)[37, 38]. The ratio of AMPAR/NMDAR currents between CART-Cre$^+$ and BD-CreER$^+$ inputs did not differ (CART: 1.15±0.09, n=61; BD: 1.36±0.11, n=52; Mann-Whitney test, $P = 0.054$), indicating comparable developmental maturation of RGC inputs labeled by the two mouse lines. Nor did tamoxifen injections in *BD;ChR2* significantly alter the function or development of the retinogeniculate synapse (Figure S3B, see STAR Methods).

TC neurons can receive inputs from multiple different types of RGCs[16, 17, 39, 40]. To begin to understand how the diversity of ooDSGCs maps onto these convergence patterns, we examined the amplitude of oEPSCs resulting from the activation of CART-Cre$^+$ or

BD-CreER$^+$ RGCs. In our recording conditions, peak AMPAR currents smaller than 600 pA cannot drive the firing of TC neurons alone in response to a single stimulus[41]. We therefore used this amplitude threshold to sort the oEPSCs we recorded into "weak" (<600 pA) and "strong" (>600 pA) inputs. We further categorized "strong" inputs that were greater than 2,000 pA as "dominant" inputs since our previously published study showed that simultaneous activation of all retinal inputs generally evokes oEPSCs that exceed this value in *Chx10;ChR2* mice [39] (Chx10 is expressed in all RGCs; Figures 3B and 3D). Recordings do not distinguish oEPSCs elicited from single versus multiple contributing RGCs. Therefore, oEPSCs correspond to the maximal summed responses of all ChR2$^+$ CART or BD RGCs synapsing onto an individual TC neuron. Most of these maximal responses were weaker than 600 pA for both CART-Cre$^+$ (69.59±7.35%, n=74 cells from 9 mice) and BD-CreER$^+$ inputs (62.44±7.11%, n=60 cells from 35 mice) (Figures 3C and 3E).

We next asked whether or not CART-Cre$^+$ and BD-CreER$^+$ inputs drive spatially distinct populations of TC neurons within this area or whether weak versus strong inputs are spatially segregated. We superimposed a grid over the parasagittal slice of the dLGN as a reference (Figure 3F) and tabulated the approximate location of each recorded TC neuron while color coding the strength of their AMPAR oEPSC (Figures 3G and 3H). Unresponsive neurons (those without a measurable oEPSC) were also annotated. In the region of axonal overlap from the two mouse lines, we found no discernable spatial pattern in TC neurons based on their responsiveness or oEPSC strength in *Cart;ChR2* mice (Figures 3G, S3D and S3E left, two-way ANOVA, $P = 0.64$). Moreover, TC neurons driven by BD-CreER$^+$ RGCs are not spatially segregated from those by CART-Cre$^+$ RGCs within the ventral-posterior territory (Figures 3H and S3E right, two-way ANOVA, $P = 0.71$).

Our finding of distinct regions in the dLGN that appear to receive BD-CreER$^+$ inputs and/or CART-Cre$^+$ raised the question of whether ooDSGCs preferring dorsal motion (labeled by *Cart;ChR2* but not *BD;ChR2* mice) exclusively innervate dLGN regions distinct from those preferring ventral motion ooDSGCs (labeled by *BD;ChR2* mice)[42]. However, this scenario could not explain our findings in Figures 3G, H. Far more sampled TC neurons were innervated by CART-Cre$^+$ inputs (~89%) than by BD-CreER$^+$ inputs (~24%) (Figures 3G and 3H). This difference cannot be simply explained by inefficient labeling in *BD;ChR2* mice, since BD-CreER$^+$ RGCs and CART-Cre$^+$ RGCs comprise ~35% and ~54% of CART$^+$ RGCs, respectively, in the retina (Figures $1C_2$ and $1D_2$ right). Taken together, our findings suggest that CART-Cre$^+$ inputs terminating in the ventral-posterior area of dLGN cannot arise just from ooDSGCs tuned to ventral motion, but that CART-Cre$^+$ inputs tuned to both ventral and dorsal motions must co-innervate this region. Therefore, axons from ooDSGCs tuned to two opposite directions appear broadly distributed across the same area.

Contribution of CART-Cre$^+$ and BD-CreER$^+$ RGCs to the total retinal drive of TC neurons

We next estimated the contribution of CART-Cre$^+$ or BD-CreER$^+$ inputs to the total retinal drive by comparing maximal amplitudes of CART/BD oEPSCs to eEPSCs from the same TC neuron (Figure 4A). The eEPSC reflects the synaptic response to the stimulation of axons from a mixed set of RGC types. In both *Cart;ChR2* and *BD;ChR2* mice, the amplitude of oEPSCs was substantially smaller than that of eEPSCs (CART: n=30 cells, $P < 0.001$;

BD: n=33 cells, $P < 0.001$; non-parametric Wilcoxon matched-pairs signed rank test; Figures 4B–C). The median ratios of oEPSC to eEPSC amplitude were 0.075 (IQR: 0.297) for CART-Cre$^+$ inputs and 0.057 (IQR: 0.38) for BD-CreER$^+$ inputs (Figures 4D left and 4E left). Factoring in the loss of axonal continuity in the slice preparation (ratio of *Chx10;ChR2* evoked oEPSC/eEPSC =~2)[39], we defined CART$^+$/BD$^+$ inputs as primary drivers when the inputs contribute to more than 50% of total retinal drive, that is, when oEPSC/eEPSC ratio is equal to or greater than 1 (see STAR Methods). Using this criterion, we observed that the majority of TC neurons receive only weak ooDSGC innervation (CART: 96.67%; BD: 84.85%; Figures 4D and 4E right). These data suggest that CART-Cre$^+$ and BD-CreER$^+$ inputs most frequently converge onto TC neurons in which the majority of their additional inputs are from other RGC types.

Role of ChR2 expression efficiency in convergence analyses

We remained concerned that the small amplitude of most ooDSGCs inputs might reflect insufficient penetrance of ChR2 expression in the two ooDSGC populations. To test this possibility, we compared the cumulative probability distributions of CART-Cre$^+$ or BD-CreER$^+$ oEPSCs with eEPSCs amplitudes, with each curve normalized to its respective population maximal oEPSC or eEPSC current. We reasoned that, even if only a small subset of vertical ooDSGC axons can be activated optogenetically, the overall cumulative distribution of optically driven responses should resemble that of eEPSCs, and to align when normalized. In fact, these normalized plots showed that the distribution of CART-Cre$^+$ and BD-CreER$^+$ oEPSCs were shifted to the left and had a different shape when compared to that of eEPSCs (Figures 5A–B, Kolmogorov-Smimov (K-S) test, $P < 0.001$). In contrast, the curve of the responses to bulk optogenetic stimulation of retinal inputs (*Chx10;ChR2*; previously published[39]) is very similar to that of the eEPSC (Figure 5C, K-S test, $P = 0.65$). These results indicate non-uniform contributions of ooDSGC inputs across the population of TC neurons and support the idea that, for the majority of TC neurons, retinal inputs recruited by electrical stimulation are not all drawn from a population of CART-Cre$^+$ or BD-CreER$^+$ RGCs inputs, but rather suggest an integration between ooDSGC and non-ooDSGC inputs.

Logic for wiring on-off directional inputs in the dLGN

At the level of an individual TC neuron dendrite, retinal boutons preferentially cluster together when their preferred directions are very similar, and, more rarely, opposite to each other[19]. Here, we asked whether synapses of ventral-preferring BD RGCs converge onto a given TC neuron with those of CART RGCs tuned to the opposite direction. To begin to address this question, we explored models of two opposite potential wiring patterns between the two CART-Cre$^+$ ooDSGC subsets and TC neurons: 1) TC neurons are innervated by convergent CART-Cre$^+$ RGC subsets that code for two different directions (Model A, Figure 6A$_1$); or 2) TC neurons exclusively receive inputs from one CART-Cre$^+$ RGC subset that codes for a specific direction (Model B, Figure 6A$_2$). Accordingly, the inputs from each subset and total CART-Cre$^+$ RGCs were simulated based on these two models (see STAR Methods). We assumed that cumulative amplitude histograms of ooDSGCs preferring ventral versus dorsal motion are very similar and can be represented by that for BD-CreER$^+$ inputs. Model A predicts that the cumulative curve of CART inputs will be significantly shifted to the right of that of BD inputs (Figure 6B$_1$, K-S test, $P < 0.001$). In

Model B, each individual TC neuron receives inputs from only one subtype of ooDSGCs, thus the distribution of synaptic responses to CART-Cre$^+$ ooDSGC inputs would be very similar to that of the ooDSGC subtype tuned to ventral motion. Our experimental data was more consistent with Model B as the distributions from the two lines were statistically indistinguishable (Figure 6C). Moreover the distribution of CART-Cre$^+$ inputs predicted by Model A (but not Model B) significantly differs from that of experimental CART-Cre$^+$ responses (versus data: Model A: $P < 0.0005$; Model B: $P = 0.67$, K-S test with Bonferroni correction).

We also modeled the impact of possible contamination of the oEPSCs in *Cart-Cre* with other RGC types (Figure S1C; 27% non-specifically labeled RGCs that may or may not also project to the sampled dLGN region). For Model A, the non-ooDSGC RGCs labeled in *Cart;ChR2* mice may converge with both CART-Cre$^+$ ooDSGC subtypes (Figure S4A$_1$) or target a distinct set of TC neurons (Figure S4B$_1$). Simulations of these scenarios yielded significantly different cumulative distribution curves between CART and BD inputs (Figures 6A$_2$ and 6B$_2$, K-S test, $P < 0.001$). Similarly, for Model B, labeled non-ooDSGCs may mix with both subtypes of vertically tuned ooDSGCs (Figure S4C$_1$) or innervate a distinct group of TC neurons than CART-Cre$^+$ ooDSGCs (Figure S4D$_1$). Our simulation for the former still predicts a shift in the distribution of CART-Cre$^+$ inputs when compared to BD inputs (Figure 6C$_2$, K-S test, $P < 0.001$). On the contrary, the latter yielded a similar cumulative distribution between vertically tuned ooDSGC inputs and ventral motion-preferring inputs (Figure 6D$_2$), consistent with functional recordings. Taken together, our data argues that the likelihood of BD-CreER$^+$ inputs converging onto the same TC neuron with the ooDSGCs preferring the opposite direction (dorsal) appears to be low.

Discussion

In mouse, neurons tuned to motion information are found in retina, dLGN and V1[26, 43–49]. Additionally, direction and orientation selectivity have been shown to be computed *de novo* in the visual cortex. How these different streams of information interact is a subject of active investigation[48–50]. To address this question, a basic understanding of how motion information from the retina is parsed in dLGN is essential. Motion selectivity in TC neurons could be inherited from the eye, consistent with a labeled line model and observations in superior colliculus[51], or computed *de novo* in the dLGN. Consistent with the latter, different information streams can converge onto the same TC neuron[16, 18, 19]. The logic of which RGC types do or do not converge and the relative strengths of these inputs is still unclear. Here, we took advantage of two *Cre* mouse lines, one labeling a subset population of the other, to identify and drive ooDSGCs inputs tuned to ventral motion direction (*BD-CreER*), and two opposite cardinal directions (dorsal and ventral, *Cart-Cre*). Our results showed that: 1) In the majority of TC neurons recorded, ooDSGC inputs contribute a small portion of total retinal drive, consistent with substantial convergence of ooDSGC inputs with other RGC types; 2) Only a small fraction of TC neurons receive primary drive from CART-Cre$^+$ or BD-CreER$^+$ inputs as would be expected in a labeled line model; 3) Analysis of our normalized cumulative probability distributions of CART-Cre$^+$ and BD-CreER$^+$ inputs suggest that subtypes of ooDSGCs tuned to dorsal and ventral motion tend not to converge onto the same TC neurons.

Convergence of directional information with other retinal inputs

Our findings indicate that most CART-Cre$^+$ and BD-CreER$^+$ inputs converge with other RGC types. We base our conclusion on the comparisons of absolute amplitudes (Figure 4) and normalized cumulative probability distributions (Figure 5) of ooDSGC-driven oEPSC versus eEPSC from the same cells. While the amplitude distributions of CART-Cre$^+$ and BD-CreER$^+$ inputs are comparable, they are strikingly different from that of input strengths obtained when we activate all convergent inputs onto a TC neuron (Figure 5). This cannot be explained simply by differences in the method of activation or ChR2 expression efficiency. First, the concentration of ChR2 in retinal axons likely reaches levels that reliably trigger action potential firing by P28, based on our previous experiments comparing the oEPSC to eEPSC amplitudes in *Chx10;ChR2* mice (described in Figure S4 of [39], see also STAR Methods). Second, as previously published[39], normalized distributions of both *Chx10;ChR2* oEPSCs (labeling the majority of RGCs with ChR2) and eEPSCs from the same cells yielded similar cumulative probability curves (Figure 5C), despite large differences in overall amplitude of oEPSC and eEPSCs attributable to axon severing in slice preparation. This aligned with the basic premise that both oEPSCs and eEPSCs in *Chx10;ChR2* mice drew on the same overall population of inputs. Taken together, these data suggest that the majority of TC neurons receiving on-off directional information are also innervated by other RGC types[16, 18, 19]. Our previous study visualizing retinal axon bouton response properties and distribution suggests that these other types may include those tuned to axis in the same direction, or those that differ in their response to luminance (On or Off)[19].

A small fraction of sampled cells did, however, have a large oEPSC/eEPSC ratio, consistent with strong ooDSGC drive that can evoke spiking. Less than 15% of responsive TC neurons received primary drive from BD-CreER$^+$ or CART-Cre$^+$ inputs, despite the axons from both of these RGC subtypes fully covering the recording area. Thus, a small fraction of TC neurons may conduct “labeled line” transmission of ooDSGC information[16, 18, 19]. Future studies should investigate the relationship between the tuning properties of the pre- and post-synaptic neurons in the dLGN and determine the functional relevance of “labeled line” convergence compared to convergent weak, nondominant heterogeneous inputs that persist even in the mature circuit.

Models of convergence of ooDSGCs

We find that ooDSGCs inputs mix with other RGC types, but how often do subtypes of ooDSGCs tuned to different directions converge onto the same relay neuron? To better address this question, we tested two simple models of convergence among different subtypes of ooDSGCs. Model A represents one end of a spectrum of connectivity patterns, where CART ooDSGCs of two opposite directions can converge onto the same TC neuron; functionally, this may correspond to a vector sum of their relative weights that contribute to the final direction that the relay neuron is tuned to. On the opposite end of the spectrum, Model B proposes that ooDSGC subtypes avoid converging onto the same TC neuron. Several predictions arise from these two models which we compared to our acquired data.

If we assume that the distribution of peak AMPAR amplitudes of oEPSCs from ooDSGCs tuned to the dorsal direction is similar to that of the ventral (BD) direction, Models A

and B predict distinct cumulative distributions (Figure 6B). The maximal oEPSC amplitude distribution for CART inputs would be shifted to the right relative to that of BD inputs if all ooDSGCs converge onto a relay neuron (Model A). In contrast, if ooDSGCs selective for vertically opposite directions avoid converging together onto the same TC neurons (Model B), we would predict that the cumulative histograms would be more similar between CART and BD. Our results show that the cumulative amplitude distribution is similar between CART-Cre$^+$ and BD-CreER$^+$ RGCs, consistent with the prediction of Model B rather than Model A. A caveat to these simulations is that they would not detect differences in the cumulative curves if contributions from one ooDSGC subtype is less than 10% of total CART-Cre$^+$— this delineates the limitations to our conclusions.

Previous studies have proposed that direction selective RGCs tuned to opposite directions may converge onto TC neurons to create orientation selectivity[19, 43, 52]. Our data and modeling did not identify this as a common convergence pattern for vertically tuned ooDSGCs, as BD-CreER$^+$ inputs, representing ventral motion in the retina, tend not to converge with the other CART-Cre$^+$ ooDSGCs tuned to dorsal motion. However, this conclusion does not preclude the possibility that opposite direction convergence may occur with relatively low frequency (<10%), as observed with presynaptic calcium imaging[19], or with other direction selective ganglion cells.

How does the logic of retinal convergence emerge over development? Scenarios include molecular cues, activity-dependent refinement, or mundane sparsity of subtype inputs from the same retinotopic location as might occur towards the periphery of the visual field[12]. The latter scenario would not explain all of our findings, as we record from a region of the dLGN that represents the central and ventral area of the visual space in the azimuth and elevation axes, respectively[44]. Taken together, our data suggest that while RGC inputs tuned to different features of the visual space can converge onto common TC neurons, this mixing does not apply for *subtypes* of ooDSGCs tuned to opposite directions of motion. Overall, our findings point to a greater complexity in the rules governing convergence of different types versus subtypes of RGCs than previously understood.

STAR METHODS

RESOURCE AVAILABILITY

Lead contact—Further information and requests for resources and reagents should be directed to and will be fulfilled by the lead contact, Chinfei Chen (Chinfei.Chen@childrens.harvard.edu).

Materials availability—This study did not generate new unique reagents.

Data and code availability—The published article includes all data generated or analyzed during this study. Relevant codes for simulation analysis are available at: (https://github.com/CClabmembers/2022_CurrentBiology.git). Any additional information required to reanalyze the data reported in this paper is available from the lead contact upon request.

EXPERIMENTAL MODEL AND SUBJECT DETAILS

Animals—All animal procedures were in compliance with the NIH Guide for the Care and Use of Laboratory Animals and approved by the Institutional Animal and Care and Use Committee (IACUC) at Boston Children's Hospital. To detect the specificity of ooDSGC labeling in *Cart-IRES2-Cre-D* mice (obtained from Hongkui Zeng Lab, Allen Brain Institute)[2, 21], they were crossed with *Ai95D* floxed GCaMP6f mice (Jackson Laboratory). Mice of ages P19-P33 of either sex were used. To drive the expression of ChR2 expression in RGCs, *Cart-IRES2-Cre-D*, *BD-CreER* (obtained from Joshua Sanes Lab)[21], and *Chx10-Cre* mice (JAX 005105)[55] were crossed with fluorescently-tagged Cre-dependent ChR2-EYFP expressing mice (homozygous *Ai32* mice, JAX 012569)[56], respectively, yielding progeny expressing ChR2 and EYFP in the retina. We refer to the resulting crosses as "*Cart;ChR2*", "*BD;ChR2*", and "*Chx10;ChR2*", respectively. Tamoxifen (200 μg, Sigma) was intraperitoneally injected at P0 or P1 to *BD;ChR2* mice for labeling of BD^+ RGCs, or to *Chx10;ChR2* mice to elaborate the effect of tamoxifen on functional synaptic connectivity. Data from *BD;ChR2* mice with fewer than 200 $EYFP^+$ RGCs were excluded from analysis (Figure S2A). Male and female animals aged P27-34 were employed.

METHOD DETAILS

Tamoxifen control experiments—Since expression of ChR2 in *BD;ChR2* mice was dependent on binding of the estrogen receptor, we asked whether the presence of tamoxifen may disrupt maturation of retinogeniculate synapses. We injected tamoxifen into *Chx10;ChR2* mice, which label all RGCs[39], with the same dosing as our experiments with *BD;ChR2* mice. Both oEPSCs and electrically stimulated EPSCs (eEPSCs) exhibited similar average amplitude in tamoxifen-injected mice when compared to those without the drug injection (Figure S3B). These results alleviate concerns of deleterious effects of tamoxifen on retinogeniculate connectivity.

Two-photon calcium imaging of CART-Cre^+ RGCs

Whole-mount retina preparation: After dark adaptation for > 30 mins, mice were anesthetized with isoflurane and euthanized by decapitation. Retinas were isolated from the pigment epithelium under infrared illumination at room temperature in oxygenated Ames' medium (Sigma-Aldrich, St. Louis, MO). Retinas were cut into dorsal and ventral halves using scleral marks as identified in Wei et al., 2010[57] and mounted on top of a 3–4 mm^2 hole in a small piece of filter paper with ganglion-cell-layer-up on top (Millipore, Billerica, MA). The mounted retinas were kept in darkness at room temperature in Ames' medium bubbled with 95% O2/5% CO2 until use (0–8 hr).

Visual stimulation: A white organic light-emitting display (OLEDXL, eMagin, Bellevue, WA; 800 × 600 pixel resolution, 60 Hz refresh rate) was controlled by an Intel Core Duo computer with a Windows 7 operating system and was presented to the retina at a resolution of 1.1 μm/pixel. Moving bar stimuli were generated by MATLAB and the Psychophysics Toolbox[58], and projected through the condenser lens of the two-photon microscope onto the photoreceptor layer. For the moving bar stimulus, a positive-contrast bar (275 μm wide, 660 μm long) moved along the long axis in 8 pseudo-randomly chosen directions at a speed of

550 μm/sec over a 660μm-diameter field on the retina; and four trials were recorded for each direction.

Calcium imaging of GCaMP6f fluorescence: GCaMP6f fluorescence of isolated retinas in oxygenated Ames at 32–33°C was imaged in a customized two-photon laser scanning fluorescence microscope (Bruker Nano Surfaces Division). GCaMP6f was excited by a Ti:sapphire laser (Coherent, Chameleon Ultra II, Santa Clara, CA) tuned to 920 nm, and the laser power was adjusted to avoid saturation of the fluorescent signal. Onset of laser scanning induces a transient two-photon response that adapts to the baseline in ~3 s. Therefore, to ensure the complete adaptation of this laser-induced response and a stable baseline, visual stimuli were given after 20 s of continuous laser scanning. To separate the visual stimulus from GCaMP6f fluorescence, a band-pass filter (Semrock, Rochester, MA) was placed on the OLED to pass blue light peaked at 470 nm, while two notched filters (Bruker Nano Surfaces Division) were placed before the photomultiplier tubes to block light of the same wavelength. The objective was a water immersion objective (20x, Olympus). Time series of each imaging window were collected at 17 Hz or higher.

Enucleation—To detect whether there are other sources of CART-Cre$^+$ or BD-CreER$^+$ inputs in the dLGN of *Cart-IRES2-Cre-D* and *BD-CreER* mice apart from the retina, *Cart;ChR2* and *BD;ChR2* mice were enucleated from both eyes at P20-24, and sacrificed after 8 days of enucleation. The distribution of GFP labeling in the dLGN was then analyzed and compared to control animals housed in normal light-dark cycle area and with both eyes present.

Tissue preparation and immunohistochemistry—Mice were anesthetized with 50mg/kg pentobarbital and transcardially perfused with 0.1M phosphate buffered saline (PBS) immediately followed by 4% w/v paraformaldehyde (PFA) in PBS. Retinas were dissected and post-fixed in 4% PFA for 30 min, and restored in PBS before immunostaining. Brains were post-fixed overnight in 4% PFA at 4°C and rinsed in PBS. Brain slices containing dLGN were coronally sectioned through Leica VT1000 vibratome with thickness of 60 μm. Following *in vitro* electrophysiology experiments, retinas and parasagittally sectioned brain slices (250 μm) were also collected, incubated in 4% PFA for 20 min, and stored in PBS until immunostaining, thus to confirm the density and specificity of labeling after each experiment.

In whole-mount retinas, we identified RGCs by the expression of RBPMS[59], and immunostained for CART and GFP (Figures 1C$_1$ and D$_1$). For retinal staining, dissected whole mount retinas were blocked in PBS containing 5% normal goat serum (NGS) and 0.1% Triton X-100 at room temperature for 1 hr. Then primary antibodies were applied in PBS containing 0.5 % Trition and 2% NGS: chicken anti-GFP (1:1000; GFP-1020, AVES Labs), rabbit anti-CART (1:2000; H-003-62, Phoenix Pharmaceuticals), guinea pig anti-RBPMS (1:1000; a gift from from Zhigang He's lab[60]) at 4°C for 2–3 days. After rinsing with 0.1% Triton/PBS, retinas were incubated with secondary antibodies at 4°C for another 2–3 days: goat anti-chicken antibody conjugated to Alexa Fluor 488 (1:1000; A11039, Invitrogen), goat anti-rabbit 555 (1:1000; A32732, Invitrogen), and goat anti-guinea pig 405

(1:1000; ab175678, Abcam). Retinas were then mounted and cover-slipped with Vectashield (VectorLabs H-1000).

Brain slices containing dLGN were stained with GFP and vesicular glutamate transporter (VGluT2) by incubating with rabbit anti-GFP (1:2000; ab290, Abcam) and guinea pig polyclonal anti-VGluT2 (1:2000; ab2251-I, Millipore), followed by secondary antibody incubation with goat anti-rabbit 488 (1:1000; a32731, Invitrogen) and goat anti-guinea pig 555 (1:1000; a21435, Invitrogen).

Microscopy—To measure the specificity of marker expression in CART-Cre$^+$ or BD-CreER$^+$ RGCs, images of the retina (12 fields of view taken from 3 *Cart;ChR2* or *BD;ChR2* mice each) were acquired with Zeiss LSM 700 using a 20x objective to detect the signals of GFP, CART, and RBPMS. Quantification was performed manually using ImageJ. To check the reliability of ChR2 expression in *Cart;ChR2* and *BD;ChR2* mice used for *in vitro* electrophysiology studies, retinas from these animals were collected, flat-mounted, and tile-imaged on the Nikon 80i epifluorescent scope using 10x or 20x objective. The images were then reassembled in Photoshop (Adobe), and the number of GFP$^+$ RGCs was quantified manually using ImageJ. To assess the colocalization of GFP and VGluT2 in the dLGN, brain slices containing dLGN were imaged with Zeiss LSM 700 or 710 confocal microscopes (Zeiss, Olympus) equipped with 5x-60x objectives and Leica TCS SP8 Laser Scanning Confocal (STED One) with 100X objective. Z-stack and tiling were automated with built-in functions in Zeiss imaging software on the LSM 710.

Electrophysiology—Brain slices containing the optic tracts (OTs) and dLGN were prepared as previously described[39]. Briefly, mice were anesthetized using isoflurane and decapitated into oxygenated (95% O_2; 5% CO_2) ice-cold cutting solution (in mM): 130 K-gluconate, 15 KCl, 0.05 EGTA, 20 HEPES, and 25 glucose (pH 7.4 adjusted with NaOH, 310–315 mOsm)[61]. The brain was then removed quickly and immersed in the ice-cold cutting solution for 60 seconds. To obtain slices maintaining continuity of retinogeniculate fiber inputs, parasagittal sectioning was conducted as previously described[36]. The brain was cut with a steel razor blade, then sectioned into 250 μm-thick slices in the oxygenated ice-cold cutting solution using a sapphire blade (Delaware Diamond Knives, Wilmington, DE) on a vibratome (VT1200S; Leica, Deerfield, IL). The slices containing dLGN and OTs were allowed to recover at 30°C for 20 minutes in oxygenated saline solution (in mM): 125 NaCl, 26 $NaHCO_3$, 1.25 NaH_2PO_4, 2.5 KCl, 1.0 $MgCl_2$, 2.0 $CaCl_2$, and 25 glucose (pH 7.4, 310–315 mOsm).

Whole-cell patch clamp was conducted on TC neurons located in the ventral posterior region of the dLGN under room temperature (lateral or middle section in Figure 2B). Cells were visualized through a monitor with projection from the camera of a DIC-equipped microscope (Olympus). Glass pipettes (Drummond Scientific) were pulled on Sutter p87 Flaming/Brown micropipette puller (Sutter Instruments), and filled with internal solution containing (in mM): 35 CsF, 100 CsCl, 10 EGTA, 10 HEPES, and L-type calcium channel antagonist 0.1 methoxyverapamil (pH7.3, 290–300 mOsm) to optimize the pipette resistance to be 1.5–2.0 MOhm. Patch recordings were performed using a MultiClamp 700B (Axon Instruments, Foster City, CA), filtered at 1kHz, and digitized at 4–50 kHz with an ITC-18

interface (Instrutech). To detect potential differences in the maturation of the synaptic inputs, both AMPA and NMDA receptor (AMPAR and NMDAR)-mediated currents were obtained by holding the membrane potential of recorded cells at −70 and +40 mV (Figure 3A right), respectively, since the ratio of these currents can provide information on the degree of maturation of the synapse[34]. Intertrial intervals were kept at 30 seconds. Since NMDAR currents are easily saturated, only AMPAR oEPSCs were analyzed for the following study. Access resistance was monitored throughout the experiment and evaluated in offline analysis. Experiments with access resistance changing over 20% were removed from analysis. To isolate excitatory synaptic currents, cells were recorded at room temperature in oxygenated saline solution containing 20 μM of bicuculline (GABAAR antagonist), 2 μM of CGP55845 (GABABR blocker), 10 μM of DPCPX (antagonist of A1 adenosine receptors), and 50 μM of LY341495 (blocker of presynaptic group II mGluRs)[37, 62–65], to block inhibitory circuits and neurotransmitter receptors that modulate retinogeniculate transmission[37, 38].

To obtain ChR2-evoked EPSC (referred to as “oEPSC”), recorded slices received a single pulse of full-field illumination of blue light through a water immersion 60x objective (Olympus LUMplanFL N 60x/1.00W), which was set at the distance where the cells and labeled axons could be visualized clearly. The blue light (470 nm, 83 mW/mm^2) was supplied by a CoolLED pE unit, lasting for 0.2 msec at highest power (100%, 83 mW/mm^2) to obtain maximal oEPSC. To assess whether the post-synaptic responses can be saturated under the highest power, responses evoked by different light power were normalized to the maximal amplitude from each animal and averaged and then plotted as a function of light intensity (Figure S3A, left).

To obtain electrical stimulated EPSC (referred to as “eEPSC”), a pair of electrodes were filled with saline solution, and lowered onto the slices. One of the electrodes was inserted into the OTs to electrically stimulate the retinogeniculate inputs. The other electrode was immersed in the bath but did not touch the brain slice, serving as the ground. Electrical stimuli were supplied by a stimulus isolator (WPI A365) delivering a 0.2 msec pulse with 200 μA for maximal eEPSC. Maximal eEPSC amplitude was determined from the average of 3–5 trials. All eEPSCs reached a saturating response when ≥ 200 μA of electrical stimulation was applied (Figure S3A right).

QUANTIFICATION AND STATISTICAL ANALYSIS

Calcium imaging analysis—Analysis was performed using ImageJ and MATLAB. Raw frames were uploaded onto ImageJ software in which regions of interest (ROIs) were manually drawn to enclose the soma of each GCaMP6f expressing cell and for a background region where there was no detectable GCaMP6f expression. These manually selected ROIs were then imported into MATLAB, where custom written scripts were used to calculate the average intensity over time for all ROIs. In MATLAB, the background trace was subtracted from the light responsive somatic traces to remove noise. Background subtracted traces were smoothed using an averaging sliding window of 3 datapoints (approximately 90–150 ms depending on framerate). We then fitted the baseline fluorescence over time to single or two-term exponential decay function using datapoints corresponding to the time between

each moving bar sweep (4 seconds). Using the fitted F0 traces, raw fluorescence data was transformed to $\Delta F/F_0 = (F-F_0)/F_0$. Traces were then resampled to 75 Hz through boxcar method and smoothed using an average sliding window of 5 data points (~ 67 ms). $\Delta F/F_0$ traces were then clipped, sorted by visual stimulus direction, and averaged over the 4 trials.

Prior to further analysis, traces were subjected to a response quality test $QI = \frac{Var(\langle Trial \rangle_1^4)_{time}}{\langle Var(Trial)_{time} \rangle_1^4}$ to ensure consistency across trials[3]. If all trials are identical such that the mean response is a perfect representative of the response, QI is equal to 1. On the other hand, if all trials are completely random with fixed variance (so that the mean response is not informative about the individual trial responses), QI falls towards $\frac{1}{num.trials}$. We implemented a quality threshold of QI ≥ 0.40 for the response from a given cell to be considered for further analysis.

The 660 μm long bar allows for clear separation between responses to the leading and trailing edge of the moving bar. Cells showing responses to the leading edge were classified as ON, cells showing responses to the trailing edge were classified as OFF, and cells showing responses to both leading and trailing edges were classified as ON-OFF. Tuning curves were plotted using the average $\Delta F/F_0$ for each direction.

For each cell, we calculated DSI = $\frac{R_{Pref} - R_{Null}}{R_{Pref} + R_{Null}}$, where R_{pref} is the cell's response at the preferred direction (i.e., maximal response), and R_{Null} is the cell's response to the direction opposite to the preferred one. Cells with DSI ≥ 0.4 were identified as direction selective. Additionally, gDSI or vector sum was calculated as $gDSI = \sum R_\theta e^{i\theta} \Big/ \sum R_\theta$ and the preferred direction was determined as the angle of the vector sum $\varphi = \arg\left(\sum R_\theta e^{i\theta}\right)$. Similarly, orientation selectivity was tested using OSI = $\frac{\sum R_{Pref} - \sum R_{Null}}{\sum R_{Pref} + \sum R_{Null}}$, where R_{Pref} and R_{Null} correspond to responses along the preferred and null axes. gOSI was calculated as $gOSI = \sum R_\theta e^{i2\theta} \Big/ \sum R_\theta$. Cells with OSI ≥ 0.4 were identified as orientation selective. Cells with DSI < 0.4 and OSI < 0.4 were classified as broadly tuned. Lastly, cells with negative-going $\Delta F/F_0$ responses during the duration of the moving bar stimulus were identified as suppressed-by-contrast.

To determine which subtypes of ooDSGCs (nasal-, temporal-, ventral-, and/or dorsal-preferring) are represented in the *Cart-IRES2-Cre-D* mouse line, we used a similar clustering algorithm described in previous studies[66, 67]. In short, K-means clustering was used to group the preferred directions of identified ooDSGCs (by criteria described above) into predetermined number of clusters (n = 2–6 clusters). This technique assigns each datapoint to a given based on the nearest centroid, or mean value of a cluster. Then, the fitness of the number of clusters was determined by silhouette value (SV) analysis:

$$\mathrm{SV(i)} = \frac{(\mathrm{b(i)} - \mathrm{a(i)})}{\max(a(i),\ b(i))},$$

where a(i) is the average angular distance between datapoint i and all other datapoints in the same cluster and b(i) is the average angular distance between datapoint i and all other datapoints in the nearest cluster. The SV values for all datapoint were averaged for all conditions (k-means clustering with n = 2–6 clusters). An average SV value approaching 1 suggests that the data is perfectly clustered; whereas, an average SV value approaching 0 suggests the presence of clusters is ambiguous. The optimal number of clusters was determined by the largest positive difference compared to a random distribution of preferred directions.

Axonal distribution analysis—Coronal and parasagittal brain slices containing dLGN were collected from P30 mice (n = 3 mice per group). For coronal analysis, three images representative of anterior, middle, and posterior area of dLGN along the anterior-posterior axis, respectively, were selected from each mouse and stained with VGluT2 and GFP. VGluT2 signals were used to demarcate the boundaries of dLGN, allowing masking of neighboring thalamic regions in ImageJ. dLGN images showing expression of GFP were superimposed over three mice and shown as Figure 2A. To assess the distribution of GFP^+ axons at different depths, dLGN images were re-oriented to align the ventricular surface to vertical line (Figure S2B top). Signals in the dLGN were subtracted by the averaged pixel value in the neighboring posterior thalamic nuclear group which was used as background control. Every pixel remaining that was greater than 0 was binarized as 1, while those <= 0 were assigned as 0. The sum of these pixel values along the vertical line (lateral-to-medial axis) was calculated in MATLAB as cumulative GFP^+ signals at different depths (Figure S2B bottom), and binned with 2×2 μm^2 pixels. To compare the depth distributions of CART-Cre^+ and BD-$CreER^+$ inputs, the summed pixel values were graphed against the distance away from the ventricular surface as dLGN depth (Figure S2B bottom).

To align with functional recordings of dLGN neurons from parasagittal slices, the distribution of CART-Cre^+ and BD-$CreER^+$ inputs were also analyzed from parasagittal aspect. Three images representative of lateral, middle, and medial area of dLGN along the lateral-medial axis, respectively, were selected from each mouse. dLGN images showing expression of GFP were superimposed from three mice and shown as Figure 2B. For analysis of the distribution of GFP^+ axons, every pixel within the dLGN was analyzed in the same way as the coronal sections except using the thalamic reticular nucleus as background control. CART-Cre^+ terminals spanned across the lateral region of dLGN, with increasing density in ventral-posterior areas when moving to medial side of the nucleus (Figure 2B left). BD-$CreER^+$ axons were sparser but also terminated in the ventral-posterior region of dLGN across lateral-to-medial sections (Figures 2B and S2C). Similar to the analysis in the coronal orientation, one-dimensional line plots were made by calculating vertical maximal projection as summed pixels (2×2 μm^2 bins) from anterior-to-posterior of dLGN (Figure S2C top). The sum of these pixel values along dorsal-ventral axis were graphed against the distance away from the dorsal surface of dLGN (Figure S2C bottom).

Simulation of ooDSGCs innervation—Two models of $CART^+$ ooDSGC subtype innervation patterns were simulated using MATLAB. In Model A, all TC neurons received inputs of varying strengths from ooDSGCs subtypes tuned to two vertical directions (dorsal

and ventral motion). In Model B, TC neurons received inputs of varying strengths from just one of the two ooDSGC subtypes. We assumed that the expression of ChR2 is not biased by the strength of a RGC input (and vice versa) and that the responses of TC neurons to the inputs from the two ooDSGC subtypes shared similar cumulative amplitude distribution as those to BD-Cre$^+$ inputs at P30. In each simulation for a given TC neuron, the AMPAR amplitude from one (Model B) or from two (Model A) different subtypes of ooDSGCs was randomly chosen from the respective cumulative distribution of BD-Cre$^+$ inputs. The simulation was repeated 1000 times. The sum of the AMPAR amplitude of all CART ooDSGC was then tabulated and compared to that of BD ooDSGCs for each model. Simulation with 10,000 repeats yielded the same results in the comparison of cumulative distribution between CART and BD inputs. In other words, for Model A, responses to each ooDSGC subtype were randomly assigned to one TC neuron and summed to obtain the CART AMPAR amplitude, while in Model B, only an input from one of the two subtypes was randomly assigned to the TC neuron. Relevant codes are available (see https://github.com/CClabmembers/2022_CurrentBiology.git).

Rationale for oEPSC/eEPSC classification—We defined primary drivers of TC neuron firing based on the threshold of oEPSC/eEPSC >1 for the following reasons. If an individual TC neuron only or mainly receives retinal inputs from CART-Cre$^+$ RGCs as primary drivers (≥ 50% of contribution), one would estimate that the ratio of oEPSC to total retinal drive should be equal to or greater than 0.5. However, we had previously made a similar comparison of the amplitude of oEPSC to eEPSC (optic nerve stimulation) in mice expressing ChR2 in all RGC inputs to dLGN (*Chx10;ChR2*). We found that the peak oEPSC amplitudes are approximately two times greater than eEPSC amplitudes (ratio of oEPSC/eEPSC >1)[39], consistent with the idea that electrical stimulation in dLGN brain slices underestimates the overall retinal drive due to transected axons. Therefore, we assume the peak eEPSC amplitude represents the lower bound (half) estimate of overall retinal drive onto a TC neuron.

Data analysis and statistics—Electrophysiological data acquisition and offline analysis were performed using custom software in IgorPro (Wave-Metrics, Portland, OR). oEPSC and eEPSC amplitudes were obtained from average traces of 3–5 trials. Data calculation and statistical analysis were conducted using Prism (GraphPad Software, Inc.), JMP (SAS Institute), and Excel (Microsoft, Redmond, WA). All data sets were evaluated for normality using the Kolmogorov-Smirnov (K-S) test. For nonparametric distributions, the Mann-Whitney or Wilcoxon signed rank test were used for unpaired or paired comparison. For normally distributed data sets, the Student's t-test was used. K-S test was also used for comparison of distribution curves with (multiple populations) or without (two populations) Bonferroni correction. Box plots indicate the median (line within box), 25–75% quartile range (box), and 10–90% range (whiskers). In violin plots, median is indicated by solid line and quartiles are marked by dashed lines. All data in bar and line graphs were represented as mean±s.e.m.. For all figures, *$p < 0.05$; **$p < 0.01$; ***$p < 0.001$.

Supplementary Material

Refer to Web version on PubMed Central for supplementary material.

Acknowledgments

We thank Drs. M. Andermann, M. Do, L. Liang, J. Reggiani, and all other members of the Chen lab for helpful discussions about the project and manuscript, and S. Barry for technical assistance. We thank Dr. Hongkui Zeng from the Allen Institute for providing the *Cart-IRES-cre-D* mouse line, and Dr. Zhigang He for the RBPMS antibody. Support was provided by the NIH RO1EY013613 to C.C., T32 NS007473 to T.S., the Edward R. and Anne G Lefler Foundation Predoctoral Fellowship to E.Y.L., and NIH RO1 NS109990 to W.W.. We thank the IDDRC Cellular Imaging Core, funded in part by S10OD016453 and U54 HD090255 for access to their shared confocal microscopes.

References

1. Baden T, Euler T, and Berens P (2019). Understanding the retinal basis of vision across species. Nature Reviews Neuroscience, 1–16. [PubMed: 30518965]
2. Martersteck EM, Hirokawa KE, Evarts M, Bernard A, Duan X, Li Y, Ng L, Oh SW, Ouellette B, and Royall JJ (2017). Diverse central projection patterns of retinal ganglion cells. Cell reports 18, 2058–2072. [PubMed: 28228269]
3. Baden T, Berens P, Franke K, Rosón MR, Bethge M, and Euler T (2016). The functional diversity of retinal ganglion cells in the mouse. Nature 529, 345. [PubMed: 26735013]
4. Sanes JR, and Masland RH (2015). The types of retinal ganglion cells: current status and implications for neuronal classification. Annual review of neuroscience 38, 221–246.
5. Bae JA, Mu S, Kim JS, Turner NL, Tartavull I, Kemnitz N, Jordan CS, Norton AD, Silversmith WM, and Prentki R (2018). Digital museum of retinal ganglion cells with dense anatomy and physiology. Cell 173, 1293–1306. e1219. [PubMed: 29775596]
6. Rheaume BA, Jereen A, Bolisetty M, Sajid MS, Yang Y, Renna K, Sun L, Robson P, and Trakhtenberg EF (2018). Single cell transcriptome profiling of retinal ganglion cells identifies cellular subtypes. Nature communications 9, 1–17.
7. Tran NM, Shekhar K, Whitney IE, Jacobi A, Benhar I, Hong G, Yan W, Adiconis X, Arnold ME, and Lee JM (2019). Single-cell profiles of retinal ganglion cells differing in resilience to injury reveal neuroprotective genes. Neuron 104, 1039–1055. e1012. [PubMed: 31784286]
8. Kay JN, De la Huerta I, Kim I-J, Zhang Y, Yamagata M, Chu MW, Meister M, and Sanes JR (2011). Retinal ganglion cells with distinct directional preferences differ in molecular identity, structure, and central projections. Journal of Neuroscience 31, 7753–7762. [PubMed: 21613488]
9. Vaney DI, Sivyer B, and Taylor WR (2012). Direction selectivity in the retina: symmetry and asymmetry in structure and function. Nature Reviews Neuroscience 13, 194. [PubMed: 22314444]
10. Barlow HB, and Hill RM (1963). Selective sensitivity to direction of movement in ganglion cells of the rabbit retina. Science 139, 412–412. [PubMed: 13966712]
11. Borst A, and Euler T (2011). Seeing things in motion: models, circuits, and mechanisms. Neuron 71, 974–994. [PubMed: 21943597]
12. Sabbah S, Gemmer JA, Bhatia-Lin A, Manoff G, Castro G, Siegel JK, Jeffery N, and Berson DM (2017). A retinal code for motion along the gravitational and body axes. Nature 546, 492. [PubMed: 28607486]
13. Dhande OS, Stafford BK, Lim J-HA, and Huberman AD (2015). Contributions of retinal ganglion cells to subcortical visual processing and behaviors. Annual review of vision science 1, 291–328.
14. Glees P, and le Gros Clark W (1941). The termination of optic fibres in the lateral geniculate body of the monkey. Journal of anatomy 75, 295. [PubMed: 17104862]
15. Sherman SM, and Guillery R (1996). Functional organization of thalamocortical relays. Journal of neurophysiology 76, 1367–1395. [PubMed: 8890259]
16. Rompani SB, Muellner FE, Wanner A, Zhang C, Roth CN, Yonehara K, and Roska BJN (2017). Different modes of visual integration in the lateral geniculate nucleus revealed by single-cell-initiated transsynaptic tracing. Neuron 93, 767–776. e766. [PubMed: 28231464]
17. Morgan JL, Berger DR, Wetzel AW, and Lichtman JW (2016). The fuzzy logic of network connectivity in mouse visual thalamus. Cell 165, 192–206. [PubMed: 27015312]

18. Rosón MR, Bauer Y, Kotkat AH, Berens P, Euler T, and Busse L (2019). Mouse dLGN receives functional input from a diverse population of retinal ganglion cells with limited convergence. Neuron 102, 462–476. e468. [PubMed: 30799020]
19. Liang L, Fratzl A, Goldey G, Ramesh RN, Sugden AU, Morgan JL, Chen C, and Andermann ML (2018). A Fine-Scale Functional Logic to Convergence from Retina to Thalamus. Cell 173, 1343–1355. e1324. [PubMed: 29856953]
20. Rogge G, Jones D, Hubert G, Lin Y, and Kuhar M (2008). CART peptides: regulators of body weight, reward and other functions. Nature Reviews Neuroscience 9, 747. [PubMed: 18802445]
21. Kim I-J, Zhang Y, Meister M, and Sanes JR (2010). Laminar restriction of retinal ganglion cell dendrites and axons: subtype-specific developmental patterns revealed with transgenic markers. Journal of Neuroscience 30, 1452–1462. [PubMed: 20107072]
22. Jo A, Xu J, Deniz S, Cherian S, DeVries SH, and Zhu Y.J.F.i.n.c. (2018). Intersectional strategies for targeting amacrine and ganglion cell types in the mouse retina. 12, 66.
23. Land PW, Kyonka E, and Shamalla-Hannah L (2004). Vesicular glutamate transporters in the lateral geniculate nucleus: expression of VGLUT2 by retinal terminals. Brain research 996, 251–254. [PubMed: 14697503]
24. Huberman AD, Wei W, Elstrott J, Stafford BK, Feller MB, and Barres BA (2009). Genetic identification of an On-Off direction-selective retinal ganglion cell subtype reveals a layer-specific subcortical map of posterior motion. Neuron 62, 327–334. [PubMed: 19447089]
25. Rivlin-Etzion M, Zhou K, Wei W, Elstrott J, Nguyen PL, Barres BA, Huberman AD, and Feller MB (2011). Transgenic mice reveal unexpected diversity of on-off direction-selective retinal ganglion cell subtypes and brain structures involved in motion processing. Journal of Neuroscience 31, 8760–8769. [PubMed: 21677160]
26. Cruz-Martín A, El-Danaf RN, Osakada F, Sriram B, Dhande OS, Nguyen PL, Callaway EM, Ghosh A, and Huberman AD (2014). A dedicated circuit links direction-selective retinal ganglion cells to the primary visual cortex. Nature 507, 358. [PubMed: 24572358]
27. Bickford ME, Zhou N, Krahe TE, Govindaiah G, and Guido W (2015). Retinal and tectal "driver-like" inputs converge in the shell of the mouse dorsal lateral geniculate nucleus. Journal of Neuroscience 35, 10523–10534. [PubMed: 26203147]
28. Bickford ME, Slusarczyk A, Dilger EK, Krahe TE, Kucuk C, and Guido W (2010). Synaptic development of the mouse dorsal lateral geniculate nucleus. Journal of Comparative Neurology 518, 622–635. [PubMed: 20034053]
29. Hong YK, Park S, Litvina EY, Morales J, Sanes JR, and Chen C (2014). Refinement of the retinogeniculate synapse by bouton clustering. Neuron 84, 332–339. [PubMed: 25284005]
30. Rafols JA, and Valverde F (1973). The structure of the dorsal lateral geniculate nucleus in the mouse. A Golgi and electron microscopic study. Journal of Comparative Neurology 150, 303–331. [PubMed: 4124620]
31. Robson J, and Mason CA (1979). The synaptic organization of terminals traced from individual labeled retino-geniculate axons in the cat. Neuroscience 4, 99–111. [PubMed: 759988]
32. Wilson J, Bose N, and Sherman S (1984). Fine structural morphology of identified X- and Y-cells in the cat's lateral geniculate nucleus. Proceedings of the Royal society of London. Series B. Biological sciences 221, 411–436. [PubMed: 6146984]
33. Hamos JE, Van Horn SC, Raczkowski D, and Sherman SM (1987). Synaptic circuits involving an individual retinogeniculate axon in the cat. Journal of Comparative Neurology 259, 165–192. [PubMed: 3584556]
34. Hooks BM, and Chen C (2006). Distinct roles for spontaneous and visual activity in remodeling of the retinogeniculate synapse. Neuron 52, 281–291. [PubMed: 17046691]
35. Hong YK, Burr EF, Sanes JR, and Chen C (2019). Heterogeneity of retinogeniculate axon arbors. European Journal of Neuroscience 49, 948–956. [PubMed: 29883007]
36. Turner J, and Salt T (1998). Characterization of sensory and corticothalamic excitatory inputs to rat thalamocortical neurones in vitro. The Journal of Physiology 510, 829–843. [PubMed: 9660897]
37. Chen C, and Regehr WG (2000). Developmental remodeling of the retinogeniculate synapse. Neuron 28, 955–966. [PubMed: 11163279]

38. Chen C, and Regehr WG (2003). Presynaptic modulation of the retinogeniculate synapse. Journal of Neuroscience 23, 3130–3135. [PubMed: 12716920]
39. Litvina EY, and Chen C (2017). Functional convergence at the retinogeniculate synapse. Neuron 96, 330–338. e335. [PubMed: 29024658]
40. Hammer S, Monavarfeshani A, Lemon T, Su J, and Fox MA (2015). Multiple retinal axons converge onto relay cells in the adult mouse thalamus. Cell reports 12, 1575–1583. [PubMed: 26321636]
41. Liu X, and Chen C (2008). Different roles for AMPA and NMDA receptors in transmission at the immature retinogeniculate synapse. Journal of neurophysiology 99, 629–643. [PubMed: 18032559]
42. Reese B (1988). 'Hidden lamination'in the dorsal lateral geniculate nucleus: the functional organization of this thalamic region in the rat. Brain Research Reviews 13, 119–137.
43. Marshel JH, Kaye AP, Nauhaus I, and Callaway EMJN (2012). Anterior-posterior direction opponency in the superficial mouse lateral geniculate nucleus. Neuron 76, 713–720. [PubMed: 23177957]
44. Piscopo DM, El-Danaf RN, Huberman AD, and Niell CM (2013). Diverse visual features encoded in mouse lateral geniculate nucleus. Journal of Neuroscience 33, 4642–4656. [PubMed: 23486939]
45. Scholl B, Tan AY, Corey J, and Priebe NJ (2013). Emergence of orientation selectivity in the mammalian visual pathway. Journal of Neuroscience 33, 10616–10624. [PubMed: 23804085]
46. Zhao X, Chen H, Liu X, and Cang J (2013). Orientation-selective responses in the mouse lateral geniculate nucleus. Journal of Neuroscience 33, 12751–12763. [PubMed: 23904611]
47. Sun W, Tan Z, Mensh BD, and Ji N (2016). Thalamus provides layer 4 of primary visual cortex with orientation-and direction-tuned inputs. Nature neuroscience 19, 308. [PubMed: 26691829]
48. Kondo S, and Ohki K (2016). Laminar differences in the orientation selectivity of geniculate afferents in mouse primary visual cortex. Nature neuroscience 19, 316. [PubMed: 26691830]
49. Rasmussen R, Matsumoto A, Sietam MD, and Yonehara K (2020). A segregated cortical stream for retinal direction selectivity. Nature communications 11, 1–16.
50. Hillier D, Fiscella M, Drinnenberg A, Trenholm S, Rompani SB, Raics Z, Katona G, Juettner J, Hierlemann A, and Rozsa B (2017). Causal evidence for retina-dependent and-independent visual motion computations in mouse cortex. Nature neuroscience 20, 960. [PubMed: 28530661]
51. Shi X, Barchini J, Ledesma HA, Koren D, Jin Y, Liu X, Wei W, and Cang J (2017). Retinal origin of direction selectivity in the superior colliculus. Nature neuroscience 20, 550–558. [PubMed: 28192394]
52. Stafford BK, and Huberman AD (2017). Signal integration in thalamus: Labeled lines go cross-eyed and blurry. Neuron 93, 717–720. [PubMed: 28231456]
53. Lein ES, Hawrylycz MJ, Ao N, Ayres M, Bensinger A, Bernard A, Boe AF, Boguski MS, Brockway KS, and Byrnes EJ (2007). Genome-wide atlas of gene expression in the adult mouse brain. Nature 445, 168–176. [PubMed: 17151600]
54. Bakker R, Tiesinga P, and Kötter R (2015). The scalable brain atlas: instant web-based access to public brain atlases and related content. Neuroinformatics 13, 353–366. [PubMed: 25682754]
55. Rowan S, and Cepko CL (2004). Genetic analysis of the homeodomain transcription factor Chx10 in the retina using a novel multifunctional BAC transgenic mouse reporter. Developmental biology 271, 388–402. [PubMed: 15223342]
56. Madisen L, Mao T, Koch H, Zhuo J. m., Berenyi A, Fujisawa S, Hsu Y-WA, Garcia III AJ, Gu X, and Zanella S (2012). A toolbox of Cre-dependent optogenetic transgenic mice for light-induced activation and silencing. Nature neuroscience 15, 793. [PubMed: 22446880]
57. Wei W, Elstrott J, and Feller MB (2010). Two-photon targeted recording of GFP-expressing neurons for light responses and live-cell imaging in the mouse retina. Nature protocols 5, 1347–1352. [PubMed: 20595962]
58. Brainard DH, and Vision S (1997). The psychophysics toolbox. Spatial vision 10, 433–436. [PubMed: 9176952]
59. Rodriguez AR, de Sevilla Müller LP, and Brecha NC (2014). The RNA binding protein RBPMS is a selective marker of ganglion cells in the mammalian retina. Journal of Comparative Neurology 522, 1411–1443. [PubMed: 24318667]

60. Norsworthy MW, Bei F, Kawaguchi R, Wang Q, Tran NM, Li Y, Brommer B, Zhang Y, Wang C, and Sanes JR (2017). Sox11 expression promotes regeneration of some retinal ganglion cell types but kills others. Neuron 94, 1112–1120. e1114. [PubMed: 28641110]

61. Pressler RT, and Regehr WG (2013). Metabotropic glutamate receptors drive global persistent inhibition in the visual thalamus. Journal of Neuroscience 33, 2494–2506. [PubMed: 23392677]

62. Hauser JL, Liu X, Litvina EY, and Chen C (2014). Prolonged synaptic currents increase relay neuron firing at the developing retinogeniculate synapse. Journal of neurophysiology 112, 1714–1728. [PubMed: 24966302]

63. Yang YC, Hu CC, Huang CS, and Chou PY (2014). Thalamic synaptic transmission of sensory information modulated by synergistic interaction of adenosine and serotonin. Journal of Neurochemistry 128, 852–863. [PubMed: 24147740]

64. Kingston A, Ornstein P, Wright R, Johnson B, Mayne N, Burnett J, Belagaje R, Wu S, and Schoepp D (1998). LY341495 is a nanomolar potent and selective antagonist of group II metabotropic glutamate receptors. Neuropharmacology 37, 1–12. [PubMed: 9680254]

65. Hauser JL, Edson EB, Hooks BM, and Chen C (2012). Metabotropic glutamate receptors and glutamate transporters shape transmission at the developing retinogeniculate synapse. Journal of neurophysiology 109, 113–123. [PubMed: 23076103]

66. Bos R, Gainer C, and Feller MB (2016). Role for visual experience in the development of direction-selective circuits. Current Biology 26, 1367–1375. [PubMed: 27161499]

67. Tiriac A, Bistrong K, Pitcher MN, Tworig JM, and Feller MB (2022). The influence of spontaneous and visual activity on the development of direction selectivity maps in mouse retina. Cell reports 38, 110225. [PubMed: 35021080]

Highlights

- Most relay (TC) neurons innervated by ooDSGCs receive inputs from other RGC types
- Only a small fraction of TC neurons are primarily driven by ooDSGCs
- TC neurons tend not to receive both inputs from ventral and dorsal-tuned ooDSGCs

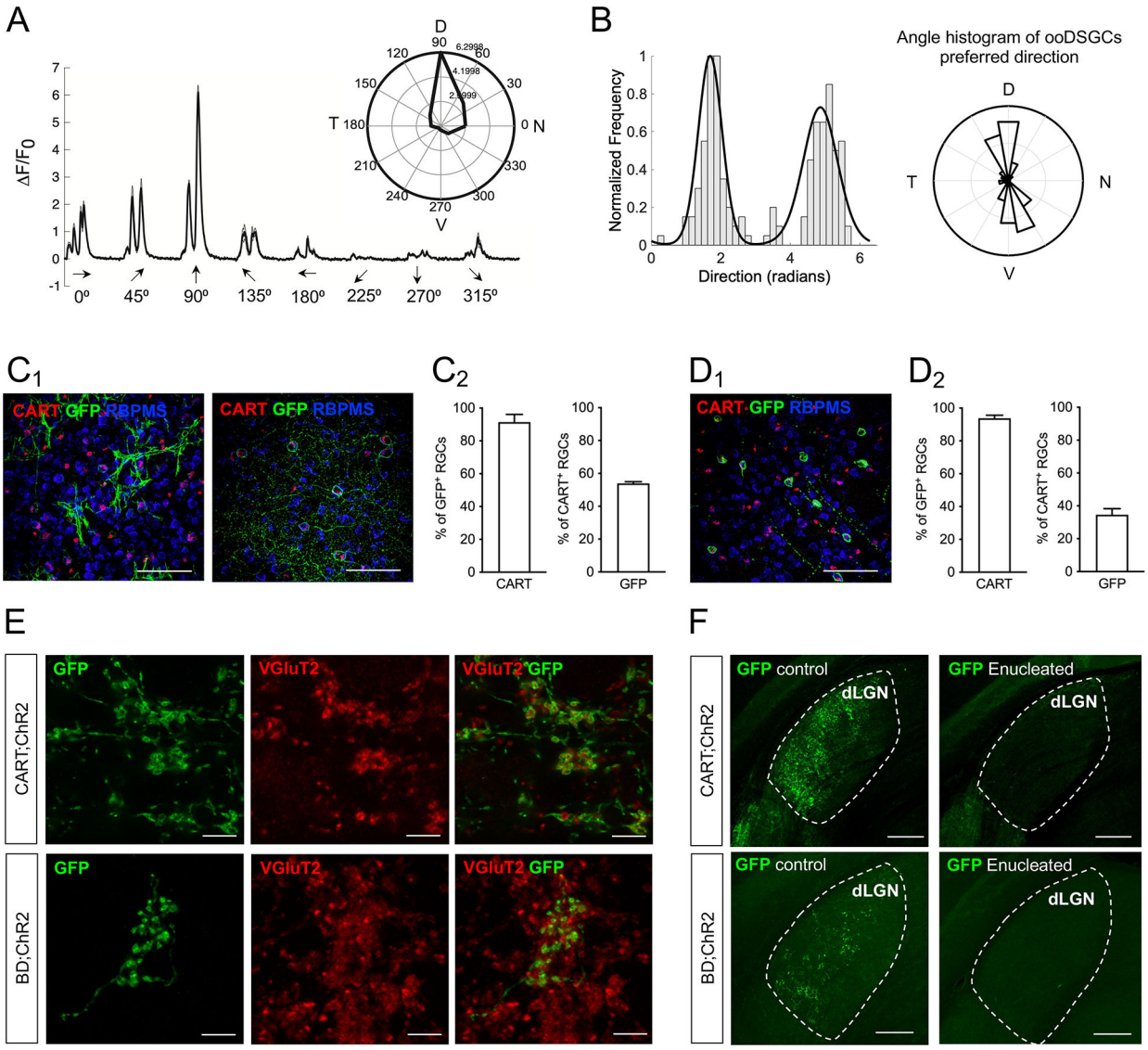

Figure 1. Specific expression of ChR2 in CART$^+$ RGCs

(A) Representative example of calcium responses to moving bars along 8 directions from one CART-Cre$^+$ RGC tuned to dorsal motion. *Inset:* polar plot. (B) Tuning distribution of CART-Cre$^+$ ooDSGCs (n=246 cells from 12 retinas, 8 mice). *Left:* Normalized frequency distribution, fit by a mixture of two Gaussian distributions (black line); *Right:* polar plot distribution showing that labeled RGCs are mainly tuned to dorsal and ventral motions. See also Figure S1. (C) Representative images from the RGC layer of *Cart;ChR2* mouse retina immunostained for GFP (green, ChR2-EYFP), RBPMS (blue, RGCs), and CART (red, ooDSRGCs) (n=4 mice). C_1 *left*: Glial cells are labeled in the *Cart;ChR2* mouse; *right*: Subsets of RGCs also express ChR2;. C_2 *left*: CART immunostaining in ChR2-expressing RGCs; *right:* ChR2 expression in CART$^+$ RGCs. (D) as in (C) but for *BD;ChR2* mouse (n=5 mice). (E) Confocal images of ChR2-expressing axonal boutons in the dLGN co-immunostained for GFP and vGluT2 in *Cart;ChR2* (*top*) and *BD;ChR2* (*bottom*) mice. (F) ChR2-expressing axonal boutons in the dLGN of enucleated mice. *Left*: normally-reared

mice; *Right*: bilaterally enucleated mice (STAR Methods) from *Cart;ChR2* (*top*, n=3) and *BD;ChR2* mice (*bottom*, n=3). Scale bars, panels: C,D: 100 μm; E: 5 μm; F: 200 μm.

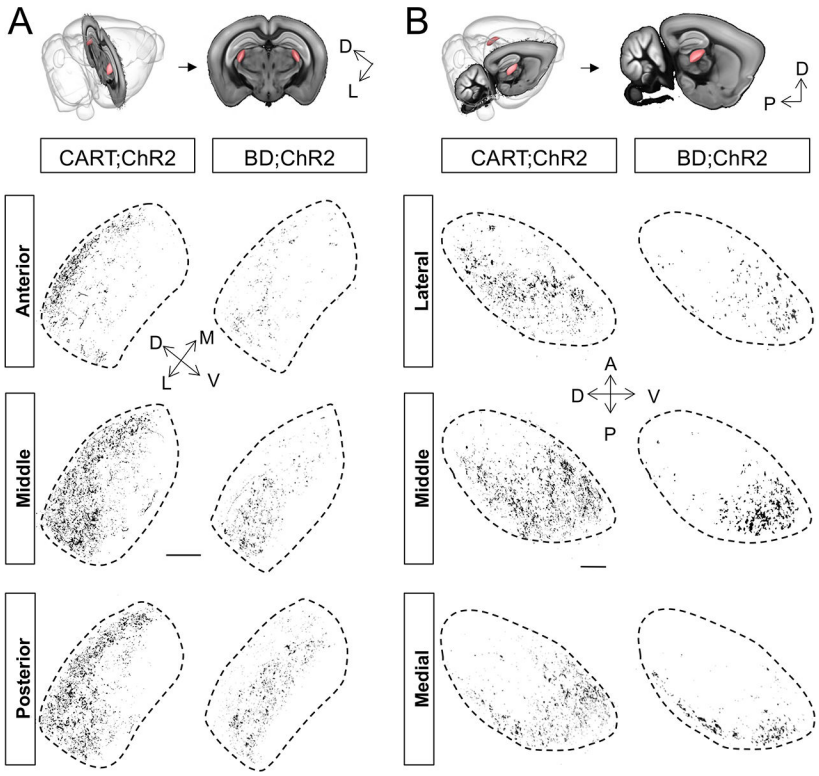

Figure 2. Distinct terminal labeling of CART-Cre^{+} and BD-CreER^{+} RGC axons in the dLGN

(A) Distribution of ChR2-expressing axons in coronal dLGN sections. *Top*: Schematic for coronal slices (from Scalable Brain Atlas[53, 54], STAR Methods); *Bottom*: coronal slices from anterior, middle, and posterior dLGN of *Cart;ChR2* (*left*, n=3 mice) and *BD;ChR2* (*right*, n=3) mice. (B) Like (A) but from parasagittal sections from lateral, middle, and medial dLGN (n=3 mice each for *Cart;ChR2* and *BD;ChR2* mice). Scale bars A, B: 200 μm. See also Figure S2, STAR Methods.

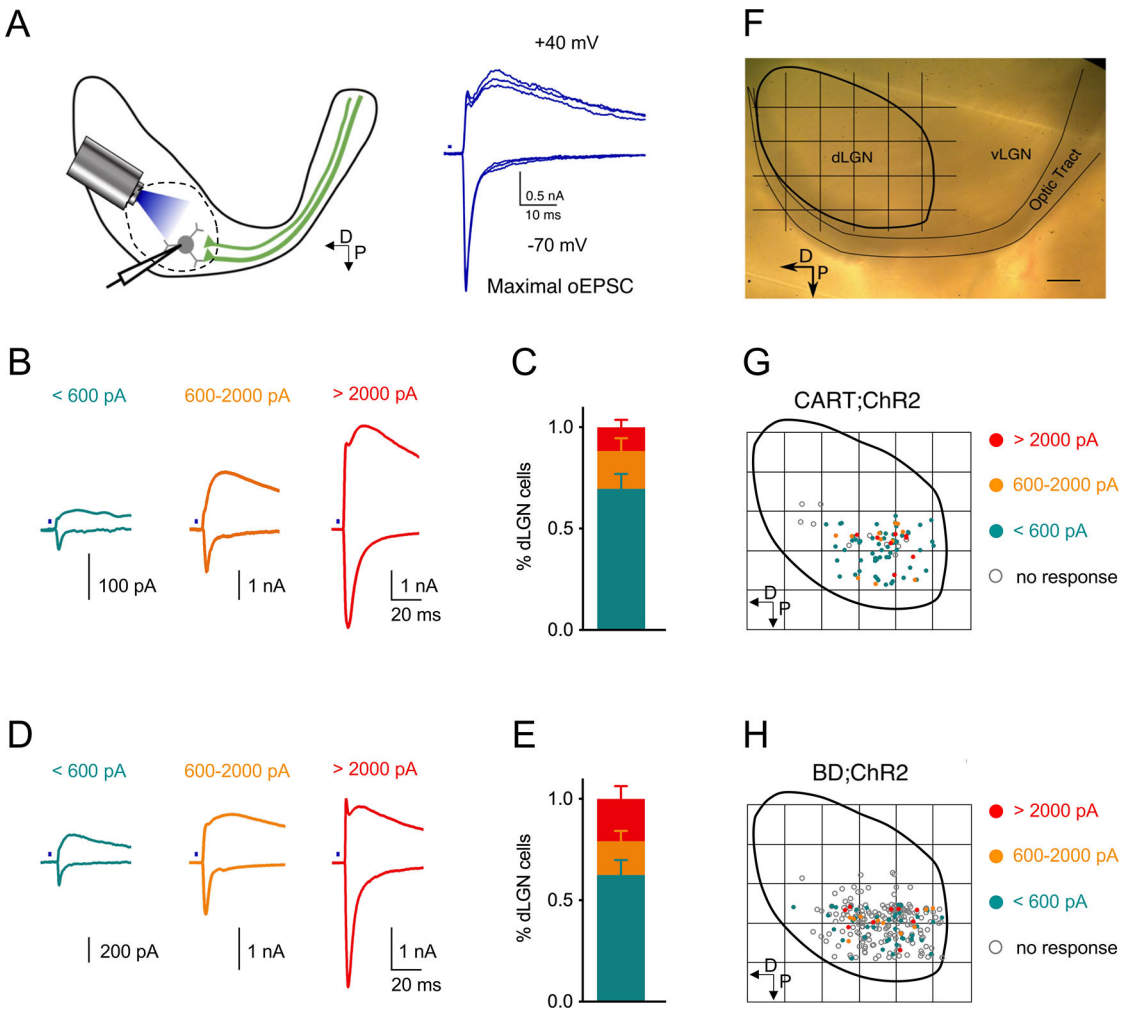

Figure 3. Synaptic properties and spatial distribution of CART-Cre$^+$ and BD-CreER$^+$ inputs

(A) Experimental protocol. *Left:* Schematic diagram of oEPSC recordings obtained from TC neurons locating in ventral-posterior region outlined by dashed curve; *Right*: Example traces of maximal AMPAR and NMDAR oEPSC (holding potential −70 and +40 mV, respectively). (B) Example traces of maximal CART-Cre$^+$ oEPSCs classified in three groups based on amplitude: less than 600 pA, large amplitude between 600–2000 pA, and dominant inputs larger than 2000 pA. The traces are color coded for classification in C, G. (C) Distribution of CART-Cre$^+$ AMPAR oEPSC amplitudes (n=74 cells from 9 mice). (D-E) Same as B, C for maximal BD-CreER$^+$ oEPSCs (n=60 cells from 35 mice). (F) Grid superimposed over dLGN image allows mapping of the approximate location of recorded neurons. (G, H) Spatial distribution of CART-Cre$^+$ (n=93 cells) and BD-Cre$^+$ responses (n=318 cells). Scale bar F: 200 μm. See also Figure S3, STAR Methods.

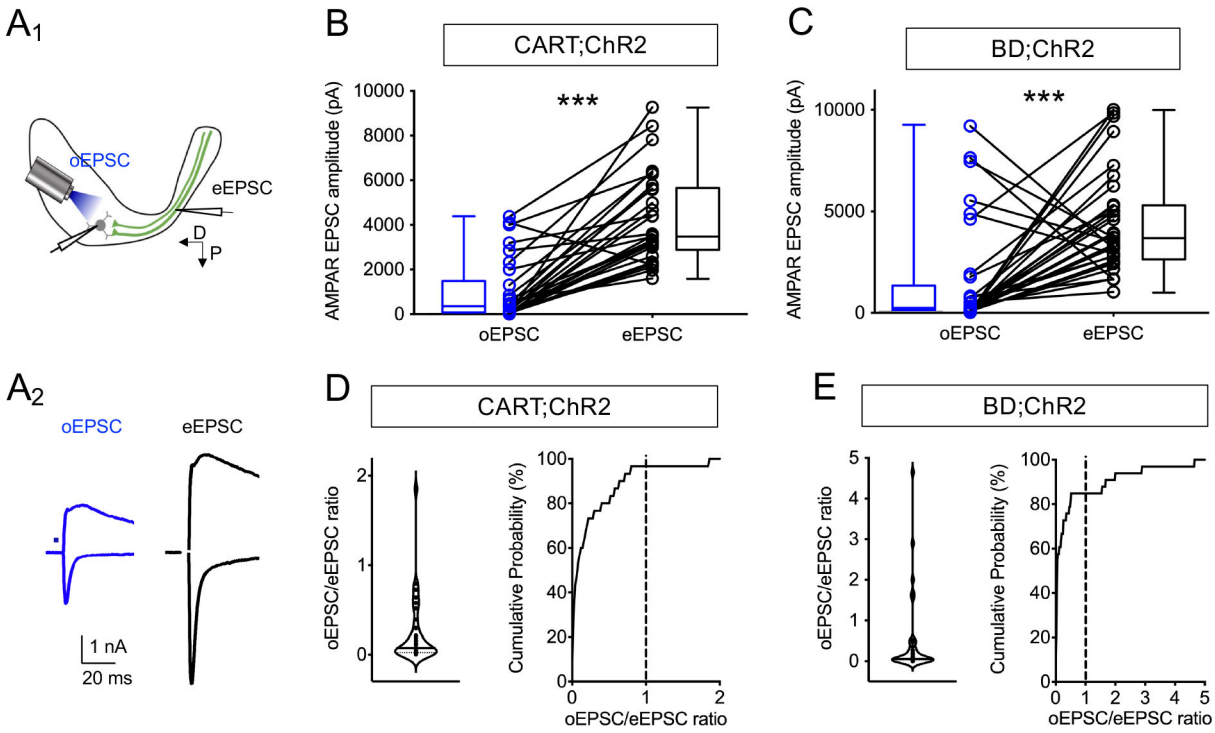

Figure 4. Contribution of CART-Cre$^+$ and BD-CreER$^+$ inputs to total retinal drive

(A) Recording of maximal oEPSCs and electrical EPSCs (eEPSCs). A_1: Schematic diagram; A_2: Example traces of maximal oEPSC and eEPSC from the same cell. (B, C) Comparison of maximal AMPAR oEPSCs to eEPSCs from the same TC neuron for CART-Cre$^+$ inputs (n=30 cells, 9 mice) and BD-CreER$^+$ inputs (n=33 cells, 19 mice). *** $P < 0.001$ Wilcoxon matched-pairs signed rank test. (D, E) Median distribution of oEPSC/eEPSC ratio in the two mouse lines. *Left*: Violin plot of oEPSC/eEPSC ratio, median is indicated by solid line, quartiles by dashed lines. *Right*: Cumulative probability distribution of oEPSC/eEPSC ratio, where primary drivers are defined as inputs with oEPSC/eEPSC>1 (vertical dashed line: ratio=1).

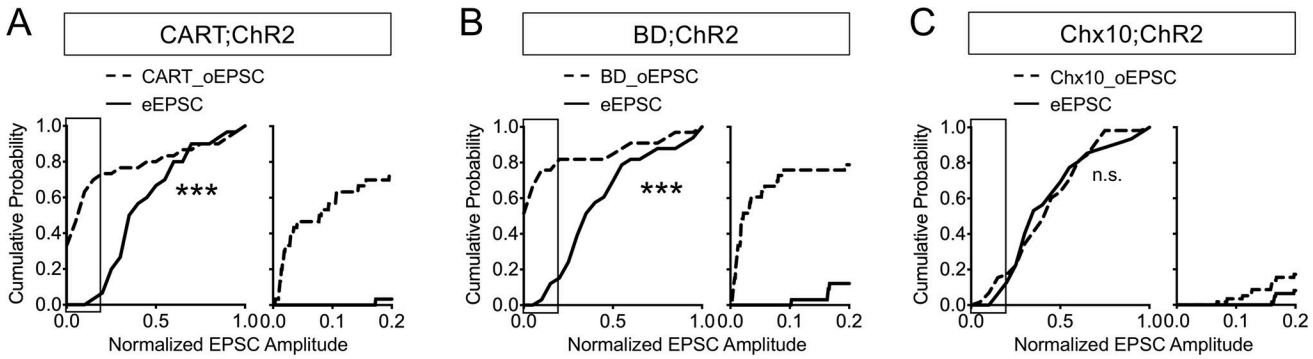

Figure 5. Comparison of amplitude distributions for different RGC inputs

Cumulative probability distribution of oEPSC and eEPSC amplitudes (normalized to the maximal current in each respective group) for CART-Cre^{+} (A, n=30 cells), BD-CreER^{+} (B, n=33 cells) and Chx10-Cre^{+} (C, n=58 cells, from data obtained from [39]). *Right*: Expanded amplitude scale corresponding to the box in the *left* panel. *** $P < 0.001$, n.s.: $P = 0.65$, Kolmogorov-Smirnov test.

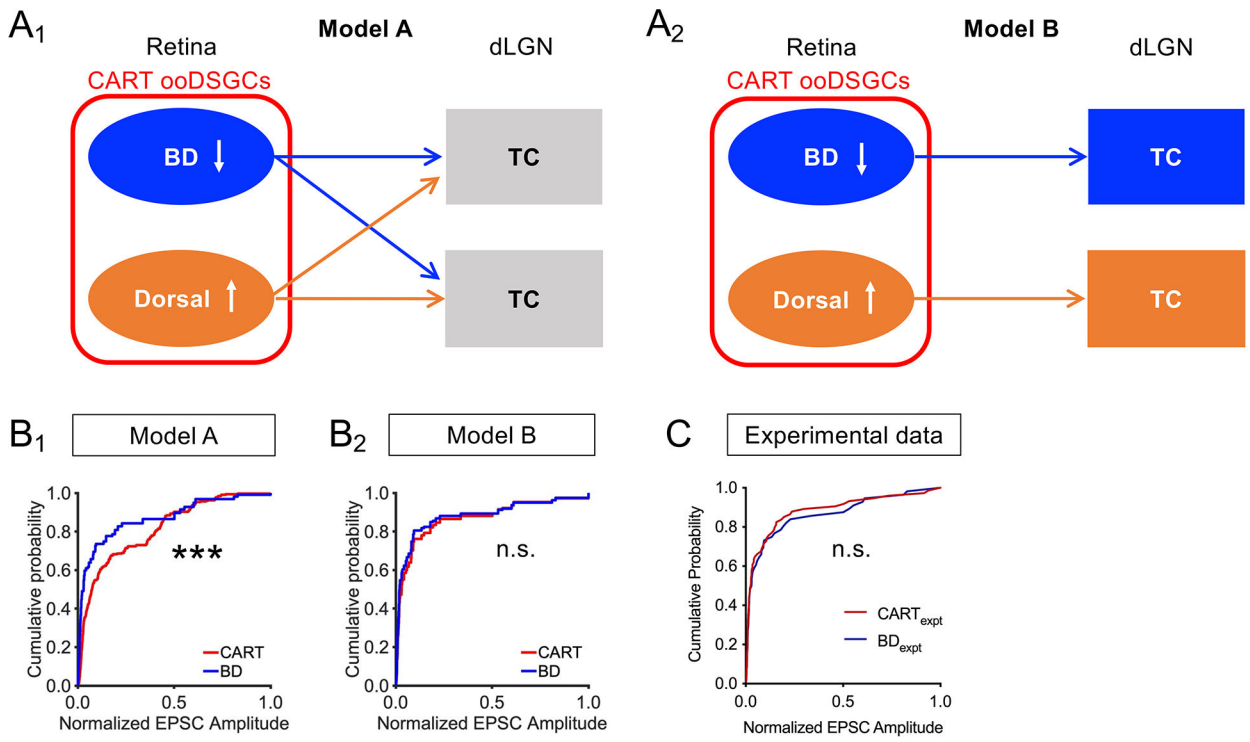

Figure 6. Modeling convergence of CART-Cre$^+$ and BD-CreER$^+$ inputs in the dLGN.

(A) Possible models of innervation by two CART-Cre$^+$ RGC subsets onto TC neurons. A_1: TC neurons receive convergent inputs from CART$^+$ RGCs tuned to two opposite directions (Model A). A_2: TC neurons are innervated by CART$^+$ RGCs tuned for a specific direction (Model B). (B) Simulated normalized cumulative probability curves based on Model A (B_1) or Model B (B_2) (See STAR Methods). (C) Comparison of normalized cumulative probability distribution from our experimental (expt) data (BD_{expt}, n=60 cells and $CART_{expt}$, n=74 cells). This data set includes cells from Figure 4 as well as those acquired in experiments without paired eEPSC measurements. *** $P < 0.001$, K-S test. See also Figure S4, STAR Methods.

Key resources table

REAGENT or RESOURCE	SOURCE	IDENTIFIER
Antibodies		
Chicken anti-GFP	AVES Labs	Cat# GFP-1020; RRID:AB_10000240
Rabbit anti-CART	Phoenix Pharmaceuticals	Cat# H-003-62; RRID:AB_2313614
Guinea pig anti-RBPMS	Zhigang He's Lab[59,60]	N/A
Goat anti-chicken IgY (H+L) (Alexa Fluor 488)	Invitrogen	Cat# A11039; RRID:AB_2534096
Goat anti-rabbit IgG (H+L) (Alexa Fluor Plus 555)	Invitrogen	Cat# A32732; RRID:AB_2633281
Goat anti-guinea pig IgG H&L (Alexa Fluor 405)	Abcam	Cat# ab175678; RRID:AB_2827755
Rabbit anti-GFP	Abcam	Cat# ab290; RRID:AB_303395
Guinea pig polyclonal anti-VGluT2	Millipore	Cat# AB2251-I; RRID:AB_2665454
Goat anti-rabbit IgG (H+L) (Alexa Fluor Plus 488)	Invitrogen	Cat# A32731; RRID:AB_2633280
Goat anti-guinea pig IgG (H+L) (Alexa Fluor Plus 555)	Invitrogen	Cat# A21435; RRID:AB_2535856
Deposited data		
Schematics in Figure 2	Scalable Brain Atlas[53, 54]	https://scalablebrainatlas.incf.org/composer/?template=ABA_v3
Code for simulations in Figure 6 and S4	This paper	https://github.com/CClabmembers/2022_CurrentBiology.git
Chemicals, peptides, and recombinant proteins		
(+)-Bicuculline	Tocris	Cat# 0130
CGP 55845 hydrochloride	Tocris	Cat# 1248
DPCPX	Tocris	Cat# 0439
LY341495	Tocris	Cat# 1209
Tamoxifen	Sigma	Cat# 85256
Experimental models: Organisms/strains		
Mouse: Cart-IRES2-Cre-D	Hongkui Lab, Allen Brain Institute[2, 21], now available in the Jackson Laboratory	Cat# 028533; RRID:IMSR_JAX:028533
Mouse: Ai95D	The Jackson Laboratory	Cat# 028865; RRID:IMSR_JAX:028865
Mouse: BD-CreER	Joshua Sanes's Lab[21]	
Mouse: Chx10-Cre	The Jackson Laboratory[55]	Cat# 005105; RRID:IMSR_JAX:005105
Mouse: Ai32	The Jackson Laboratory	Cat#012569; RRID:IMSR_JAX:012569
Software and algorithms		
MATLAB_R2019b	Mathworks	https://www.mathworks.com/products/matlab.html; RRID:SCR_001622
ImageJ (Fiji)	NIH – public domain	https://imagej.net/Fiji; RRID:SCR_002285
Igor Pro	WaveMetrics	https://www.wavemetrics.com/products/igorpro; RRID:SCR_000325
Prism 8	Graphpad	https://www.graphpad.com/scientific-software/prism/; RRID:SCR_005375

REAGENT or RESOURCE	SOURCE	IDENTIFIER
JMP	SAS Institute	http://www.imp.com/en_us/software/jmp.html; RRID:SCR_014242